

# Advanced Finite Element Model for predicting surface integrity in high-speed turning of AA7075-T6 under dry and cryogenic conditions

S Imbrogno (✉ [stano.imbrogno@unical.it](mailto:stano.imbrogno@unical.it))

University of Calabria: Universita della Calabria

Giovanna Rotella

Antonio Del Prete

---

## Research Article

**Keywords:** Surface integrity, finite element model, AA7075-T6, machining, cryogenic

**Posted Date:** May 25th, 2022

**DOI:** <https://doi.org/10.21203/rs.3.rs-1643587/v1>

**License:** © ⓘ This work is licensed under a Creative Commons Attribution 4.0 International License.

[Read Full License](#)

---

# Abstract

The overall quality of a component, its mechanical performance and reliability during all its life cycle depends on several characteristics. The choice of the material plays an important role in satisfying the requirements and usually it makes the difference between failed and not failed products, however another significant impact in the material performances is characterised by the manufacturing process.

Nowadays, the numerical simulation represents an important tool to quickly predict several scenario depending on process parameters changes leading to a more flexible manufacturing process and time-cost saving due to the reduced experimental tests. This work presents an innovative Finite Element Model (FEM) of high-speed turning of one of the most used aluminium alloys in aerospace field, namely the AA7075-T6. The developed simulation tool allowed to better investigate the metallurgical phenomena triggered by the vary process parameters tested and the cooling conditions used during the machining tests. A physics-based model to simulate the material behaviour has been developed and implemented via subroutine within the FEM software. The predictive capability of the model has been validated through experimental and numerical comparison of cutting forces, maximum temperature and the grain size changes.

## 1. Introduction

Dictating the functional performance and service-life of a component, surface integrity plays a key role in the current industrial market since product quality competes with cost reduction and it is critical to achieve by current technologies [1]. One of the most relevant industrial examples is the aircraft industry where surface integrity of components is of undeniable interest being the driving force of a reliable, safe, and suitable component. As one of the most used process, machining is drawing attention as the finishing process able to manufacture components complying with such required standards. In fact, as the product requirements become more demanding, post operations able to correct and improve the final machined surface characteristics are needed since not enough knowledge on how to properly modify the finishing process to obtain the desired product performance are available. It is necessary to study the mechanics of the process coupled with the physics driving product changes and surface integrity variations in order to accurately tune it by modifying the process characteristics. Thus, accurate models capable of describing such phenomena need to be defined in order to obtain useful information on how to improve the selected machining process manufacturing reliable products increasing the knowledge-driven manufacturing process planning, as well as better prediction of the component's lifetime [2]. Simplified models based on empirical formulations describing materials characteristics and behaviour during machining are not useful to explain the real materials constitutive law even though simplified models are applicable into a certain constraint [3–5]. Therefore, an accurate physics-based model is presented herein to describe the microstructural and integrity evolution of AA7075 aluminium alloy machined under dry and cryogenic conditions. The FEM allows to investigate the metallurgical phenomena that are taking place during the process and being able to predict the material's changes during the process.

Thus, it is possible to properly set up the process in order to modify it according to the desired product quality characteristics tremendously reducing the required time and efforts related to expensive process experimental campaign. Furthermore, the design of the implemented model can give detailed explanation on how each considered factor will contribute to the overall material's changes answering to questions which are not possible to resolve analysing the experimental results.

## 2. Material

The material investigated in this study was the aluminium alloy AA7075-T6 (wrought condition) provided as cylindrical bars (100mm diameter and 360mm length). The high-speed machining (HSM) tests, in particular turning operation, were conducted on a CNC lathe machine (Mazak Quick Turn II) and two manufacturing conditions i.e. dry and cryogenic were investigated. The machining parameters such as cutting speed and feed rate, were varied on three (1000 m/min, 1250 m/min and 1500 m/min) and two levels (0.1 mm/rev and 0.3 mm/rev) respectively, while the depth of cut was kept constant and equal to 2 mm. The parameters were defined according to the Sandvik guideline for machining aluminium and its alloy. The model of the tool holder was SSDCL 2020K 09 and the tool was SCMW 09 T3 04 H13A, both provided by Sandvik Coromant©. The thermal field within the cutting zone and the cutting forces were acquired through an infrared (IR) camera and a piezoelectric dynamometer respectively. Detailed information about the experimental activities and the set up used are reported in [6].

## 3. Physics Based Constitutive Model

The constitutive law considered to simulate the material behaviour during machining processes was developed taking into account the experimental observation of Ma et al. 2014, Dixit et al. 2008 and Zhao et al. 2004 [7–9]. When a physics based model is considered, the comprehensive understanding of the material characteristics and all the physics variables that can contribute to describe the mechanical strengthening phenomena are fundamentals. Taking into account the aluminium alloy 7xxx series, the elements Zn, Mg and Cu form precipitates of various ternary and quaternary compositions following solution heat treatment and aging. The strengthening effects of these precipitates depend on their size, spacing and distribution. Other mechanisms like grain boundary strengthening, solid solution strengthening and strengthening due to work hardening contribute to increase the strength [8]. Therefore, regarding the aluminium alloy AA7075-T6, the aforementioned mechanisms strengthening were taken into account during the formulation of the physically-based material behaviour model. As stated by Kocks 1966 [10] and subsequently from many other researchers [11–14] the yield strength can be reasonably assumed as a linear additivity of the different strengthening contributions previously mentioned (Eq. 1).

$$\sigma = \sigma_{th} + \sigma_{dis} + \sigma_{hp} + \sigma_{or} + \sigma_{ss}$$

Where  $\sigma_{th}$  is representative of the short-range contribution and is thermally activated. It is the stress needed for a dislocation to pass short-range obstacles and to move it through the lattice (also known as the general term for dislocation glide) [15]. The thermal vibrations can assist the stress to overcome these obstacles. The  $\sigma_{dis}$  denotes the long-range and it is often called strain hardening due to the forest dislocations (dislocation strengthening),  $\sigma_{hp}$  is representative of the Hall-Petch effect (long-range contribution), namely the grain size strengthening effect (i.e. grain size contribution to the flow stress). The  $\sigma_{Or}$  is representative of the precipitation hardening (short-range contribution) and the  $\sigma_{ss}$  of the solid solution hardening (short-range contribution). The long-range contributions are sometimes considered as athermal contribution because the thermal vibrations cannot assist a moving dislocation to pass the region subjected to long-range distortion of lattice [16].

### 3.1 Long-range contribution - strain hardening

The interaction between moving dislocations and immobile dislocations is a long-range interaction (if it cuts orthogonal to the dislocation is of short-range). This interaction is the physical basis of the strain-hardening of a metal. The long-range contribution to the material resistance is represented by Eq. 2 ( $\sigma_{dis}$ ). This mechanical resistance is due to the interactions with the dislocation substructure [17, 18].

$$\sigma_{dis} = M\alpha Gb\sqrt{\rho_i}; \left( G = 28815 - \frac{3440}{e^{\frac{210}{T}} - 1} \right) \quad (2)$$

In Eq. 20,  $\alpha$  is a proportional fraction,  $\rho_i$  is the density of immobile dislocations and  $G$  is the temperature dependent shear modulus,  $b$  is the Burger's vector and  $M$  is the Taylor factor computed as  $(G/G_0)$ . The immobile dislocation density evolution is described by Eq. 3 (density dislocation evolution) [19]. It is important to highlight that the mobile dislocation is assumed to be much smaller than the immobile one. The evolution equation consists of two terms:  $\dot{\rho}_i^{(+)}$  that is representative of the hardening and  $\dot{\rho}_i^{(-)}$  that is representative of the softening due to the recovery.

$$\dot{\rho}_i = \dot{\rho}_i^{(+)} - \dot{\rho}_i^{(-)}$$

3

#### 3.1.1 Hardening contribution

The mobile dislocations may encounter obstacles that prevent further movement and become immobilized due to the trapping effect of the obstacles. Moreover, when dislocations are moving next to the grain boundaries can be annihilated due to the interactions with dislocations of opposite sign. The increase in dislocation density is assumed to be proportional to the plastic strain rate (Eq. 4).

$$\dot{\rho}_i^{(+)} = \left( \frac{1}{s} + \frac{1}{D} \right) \frac{M^-}{b} \epsilon^P = \frac{M^-}{b\Lambda} \epsilon^P$$

4

M is the Taylor, b is the Burger's vector,  $\bar{\epsilon}^P$  is the plastic strain rate and  $\Lambda$  interprets the mean free path of a moving dislocation until it is immobilized. In the Eq. 4, D and s represents the grain size and the cell size respectively. The cell size is assumed to be inversely proportional to the square root of the immobile dislocation according to Eq. 5 [20].

$$s = \frac{K_c}{\sqrt{\rho_i}}$$

5

where  $K_c$  is a calibration parameter.

### 3.1.2 Softening contribution

Different processes may contribute to the reduction in the dislocation density. They are separated into static and dynamic recover as showed by Eq. 6.

$$\dot{\rho}_i^{(-)} = \dot{\rho}_{sr}^{(-)} - \dot{\rho}_{dr}^{(-)}$$

6

The  $\dot{\rho}_{sr}^{(-)}$  represents the static recovery. This formulation is depending on some physics constants as Boltzmann's constants and self-diffusivity models. It is also depending on grown of dislocation density that is used in the model to prevent that the dislocation density become zero when very long times are considered in the process. In the machining simulation, a very short interval time proportional to  $1e^{-7}$ s is considered, consequently its contribution ( $\dot{\rho}_{sr}^{(-)}$ ) was neglected. On the contrary, the dynamic recovery term  $\dot{\rho}_{dr}^{(-)}$  is proportional to the immobile dislocation density and the plastic strain rate (Eq. 7). The dynamic recovery implies that moving dislocation annihilates the immobile ones.

$$\dot{\rho}_{dr}^{(-)} = \Omega \rho_i^- \epsilon^P$$

7

where  $\Omega$  is a recovery function and its expression is reported in Eq. 8.

$$\Omega = \Omega_0 + \Omega_{r0} \left( \frac{1}{\epsilon^p} \frac{D}{b^2} \right)^{1/3}$$

8

Where  $D$  is a diffusivity, while  $\Omega_0$  and  $\Omega_{r0}$  are two calibration parameters. As reported by Bergstrom 1983, the recovery for the dislocations takes place mainly in the cell walls and this process is due to climb controlled by excess vacancies created during deformation [19].

## 3.2 Long-range contribution – the Hall-Petch effect

The Hall-Petch effect is due to the resistance to dislocation motion offered by grain boundaries. In detail, this effect is due to pile-up of dislocations at grain boundaries leading to the activation of other slip systems in the surrounding grains [21]. The equation representative of the Hall-Petch contribution to the flow stress was computed as showed by Eq. 9.

$$\sigma_{hp} = \sigma_0 + \frac{k_{hp}}{\sqrt{D}}$$

9

Where  $\sigma_0$  is the frictional or Peierls stress and its value has been taken from [22],  $D$  is the grain size and  $k_{hp}$  is a coefficient. As grains are refined progressively, once they decrease under a critical value the material strength starts to decrease. This phenomenon is commonly referred to the inverse Hall-Petch effect and different physical explanations are available in literature [23–25]. The coefficient  $k_{hp}$  catches the physics phenomenon that is particularly evident as a grain boundary sliding coupled with extreme grain refinement. This results in a softening effect on the material constitutive behaviour and this effect is captured by the Eq. 10 [11]:

$$\left\{ \begin{array}{l} k_{hp} = \alpha_G^0 \tanh \left( \frac{d}{D^{-0.5}} \right)^\nu \\ \nu = 0.000475T + 1.2455 \end{array} \right.$$

10

Where  $d$  and  $\alpha_G^0$  are calibration parameters while  $D$  is the grain size due to continuous grain refinements. The  $\nu$  is a calibration parameter depending on the temperature.

### 3.2.1 Grain size evolution

The grain size  $D$  was computed based on the Eq. 11 reported by Hallberg et al. 2010 [26]. The model was developed taking into account the inelastic deformation defined by the formation and annihilation of dislocations together with grain refinement due to continuous dynamic recrystallization. This latter occurs due to plastic deformation also without the aid of elevated temperature.

$$D = D_0 - (D_0 - D_f) \left[ 1 - e \left( -k_x (\epsilon_{eff} - \epsilon_c)^{c_x} \right) \right], D_f \leq D \leq D_0$$

11

$$\epsilon_c = 0.058556 \left( \frac{Z}{A} \right)^{0.00645}$$

12

$$Z = \dot{\epsilon}_{eff} e \left( \frac{Q}{RT} \right)$$

13

Where  $D_0$  is the initial grain size (4.85  $\mu\text{m}$ ),  $D_f$  is the final grain size (in this case is the smallest grain size measured from all the case analyzed and its value is equal to 1.54  $\mu\text{m}$ ) and  $k_x$  and  $c_x$  are numerical constants. The Eq. 11 is also depending on effective plastic strain  $\epsilon$ ,  $\epsilon_{CR}$  is the critical strain for the nucleation of the recrystallization (Eq. 12) and its formulation has been taken from Quan et al 2012 [27]. The critical strain physically represents the strain point at which the dynamic recrystallization usually starts and the Eq. 12 depends on  $Z$  that is the Zener-Hollomon parameters. The  $Z$  parameter was computed as shown by Eq. 13 and the coefficient  $A$  is a numerical constant also reported in [27].  $Q$  is the activation energy that is function of strain rate and temperature as reported by Shi et al. 2013 [28].

### 3.3 Short-range contribution

The  $\sigma_{th}$  term, showed by Eq. 14 represents the material resistance to plastic deformation due to the short-range interactions where thermal activated mechanisms assist the applied stress in moving dislocations [29]. Short-range obstacle is a general classification of any disturbance of the lattice that is "small enough" so that thermal vibrations can, together with the effective stress, move the affected part of a dislocation through that region.

$$\sigma_{th} = M\sigma_i \left( 1 - \left( \frac{k_b T}{g_{0i} G b^3} \ln \left( \frac{\dot{\epsilon}_{ref}}{\dot{\epsilon}^p} \right) \right)^{2/q} \right)^{1/p}$$

14

where  $k_b$  is the Boltzmann constant,  $T$  is the temperature,  $\Delta f_0$ ,  $q$  and  $p$  are calibration parameter and  $\dot{\epsilon}_{ref}$  is typically taken as  $10^6$  or  $10^{11}$  [30].

The  $\sigma_{or}$  represents the strengthening effect due to the precipitation hardening in the Al alloy of very small particles that usually are not sheared during the mechanical tests at yield stress (Eq. 15).

$$\sigma_{or} = 0.3MG \frac{b}{R} \sqrt{f_v}$$

15

$\sigma_{or}$  is depending on  $G$  that is the shear modulus,  $R$  is the mean particle radius of the precipitates,  $M$  that is the Taylor factor computed as  $(G/G_0)$ ,  $b$  is the Burger's and  $f_v$  is the precipitate volume fraction [31].

The  $\sigma_{ss}$  term is representative of the solid solution strengthening and generally, in metals it depends on the concentration of solute atoms dissolved in the matrix  $C$  as showed by Eq. 16.

$$\sigma_{ss} = HC^n$$

16

Where  $H$  is computed as showed by Eq. 17 and  $n$  is a constant. The parameter  $n$  can be in the range of 0.5–0.75 [32].

$$H = - 1.2004T + 885.11$$

17

As previously mentioned, there are some numerical constants that are unknown, as a result their value was calibrated by fitting the experimental true stress-true strain curve obtained. In particular, some compression tests at different temperature and at strain-rate  $0.1 \text{ s}^{-1}$  and  $0.5 \text{ s}^{-1}$  were carried out. Subsequently, the numerical predictions provided by the physically-based model were plotted together with the experimental curves and a fitting procedure was initialized. Once the fitting procedure provided an average error lower than 1%, the unknown numerical constants were finally determined. Subsequently, the model has been elaborated through excel and the numerical unknown constants were obtained after calibration procedure.

In Fig. 1 are reported the simulated curve and the experimental representative of the true stress-true strain curves. The model was able to match the experimental curves at varying temperature and strain rate. All the numerical and physics constants are reported in Table 1. It is important to highlight that the model was able to correctly replicate the mechanical behaviour at large plastic deformation values (higher than 0.3) in the region that characterizes the machining process.

Table 1  
 Numerical constants of the physics based model developed (calibrated or reported in literature).

Numerical constants	Value
$\alpha$	0.2
$b$ [m]	$2.86^{-10}$
$K_c$	21
$\Omega_0$	4.43
$\Omega_{r0}$	0.33
$\rho_0$ [ $m^{-2}$ ]	$10^{10}$
$\sigma_0$ [MPa]	0.01
$\sigma_i$ [MPa]	615
$\alpha^0_G$	3300
$d$	1
$D_0$ [ $\mu m$ ]	4.85
$D_f$ [ $\mu m$ ]	1.55
$k_x$	3.8
$c_x$	2
$k_b$ [J/K]	$1.38^{-23}$
$g_{0i}$	0.55
$q$	1.5
$p$	0.678
$R$ [m]	$1.50^{-09}$
$f_v$	0.085
$n$	0.67
$C$	0.081

Figure 2 shows the prediction strategy implemented by sub-routine into the FE software DEFORM in order to simulate the constitutive material behaviour of the aluminium alloy *AA7075-T6* during machining operations. The routine was developed in FORTRAN code, the FE software computed the routine step after step upgrading the state variable as strain, strain rate and temperature. Subsequently all the equations that represent the model were computed and the flow stress was upgraded at the end of each step. The routine returned the stress, strain, strain rate, temperature and the metallurgical variables at the end of each step.

## 4. Fe Model

### 4.1. Geometry, thermos-mechanical boundary conditions

The simulation of the machining process was carried out through the software SFTC DEFORM 3D. In detail, the region near the cutting zone was considered to reduce the computational time required by the simulation. The FE model was characterised by two elements, the tool and the workpiece both modelled by CAD software and then imported within the software DEFORM. The cutting tool was assumed as a rigid body and only the volume near the tool tip was modelled with 50000 tetrahedral elements, the density of the mesh was increased toward the tool tip to accurately model the cutting-edge radius since it affects the prediction of the thrust force. The workpiece was meshed with 110000 tetrahedral elements and a refined mesh window was set within the cutting zone to obtain a mesh element size approximately fifty times smaller than the elements outside the window. This operation allowed aiming a better accuracy of the prediction of the monitored process variables (cutting forces, temperature and metallurgical alterations).

Once defined the three-dimensional geometry, the kinematic and thermal boundary conditions were set on the tool and workpiece. In Fig. 3 the surfaces with the kinematic-thermal boundary conditions are reported. Figure 3a represents the kinematic boundary conditions on the tool and workpiece; in particular, the bottom and side surfaces of the tool were fixed in x, y and z directions while the tool was completely free to move.

The cutting speed and the feed rate were set on the tool in according with the ones used during the experimental tests. The cutting speed was set considering the x direction. Regarding the thermal boundary conditions (Fig. 3b), the upper surface of the workpiece was in contact with the air, therefore, it was able to exchange heat with the environment as the rake and flank face of the tool (green colour). The bottom and side face of the workpiece were at room temperature since represented the inner material as well as the back part of the tool (red colour). The aluminium alloy bars were also machined under cryogenic condition. Therefore, considering the cryogenic effect, a further environmental window, that thermally represents the region in which the liquid nitrogen was delivered, was considered. Inside this customized window (Fig. 3a), the temperature was set equal to  $-196^{\circ}\text{C}$  (liquid nitrogen boiling temperature) while the heat transfer convective coefficient  $h_{cryo}$  ( $\text{W}/\text{m}^2\text{K}$ ) was computed by the Eq. 18 [33].

$$h_{cryo} = \frac{0.20}{b^{0.35} g^{0.33}} \frac{V_f^{0.65} k_f^{0.67} c_p^{0.33} \gamma_f^{0.33}}{v_f^{0.32}}$$

18

where;  $b$  is the equivalent length (m),  $g$  is the gravitational acceleration ( $m/s^2$ ), and the remaining parameters are properties of the fluid, namely:  $V_f$  is the velocity (m/s),  $k_f$  is the thermal conductivity (W/m K),  $\gamma_f$  is the specific weight ( $kg/m^3$ ),  $v_f$  is the dynamic viscosity (Pa\*s) and  $c_p$  is the specific heat capacity (J/kg K). As reported by Pušavec et al. 2016 [34], the physical properties of the liquid nitrogen are mostly depending on the temperature, therefore Eq. 18 can be entirely expressed as a function of the temperature. Therefore, the value of  $k_f$ ,  $v_f$ ,  $c_p$  and  $\gamma_f$  depending on the temperature were extrapolated from [34] and implemented in Eq. 18 to represent the heat transfer convective coefficient  $h_{cryo}$  as a function of the temperature (Eq. 19).

Based on this equation and considering the physical and thermal properties of the liquid nitrogen, the Eq. 19 was determined depending on the temperature (Fig. 4) and implemented in the FE software. The shape of the curve represented in Fig. 4 was due to the presence of transition of the nitrogen from liquid to gas (in corresponding to the  $-196^\circ C$ ). As reported by Pušavec et al. 2016 [34], the knowledge of the condition of nitrogen is fundamental to better understand its physic characteristics such as density, specific heat capacity, viscosity and therefore its ability to provide benefits into the cutting zone. In Fig. 4 are reported the nitrogen properties depending on the temperature. There are significant differences before and after the boiling temperature, consequently the cryogenic characteristics are strongly affected by the liquid or gas nitrogen phase. Correlating these aspects with the cooling capacity/capability, of different nitrogen phases, it must be considered that when nitrogen is delivered to the cutting zone in the liquid phase, a larger amount of the heat is used due to its more favourable physical properties [34].

Depending on the temperature and consequently on the liquid or gas phase the heat transfer coefficient set into the customized heat exchange window is described by the following equations.

$$h_{cryo} = \begin{cases} 0.07042T^2 + 42.08T + 7737, & T < -196^\circ C (\text{Liquid phase}) \\ 0.03495e^{-0.3282T} + 224.9, & T \geq -196^\circ C (\text{Gas phase}) \end{cases}$$

19

To proper simulate the interaction between the tool and the workpiece within the chip-tool interface, a hybrid friction model representative of a combination of sticking-sliding phenomena that occur in this region was employed. In detail, the sticking-sliding friction model (sticking governed by the shear model  $\tau = m\tau_0$  sliding governed by the Coulomb model  $\tau = \mu\sigma$  were also implemented), and the value of  $m$  and  $\mu$  were calibrated according to prior results on the cutting forces [35–37].

## 4.2. Calibration strategy

The calibration procedure aimed to determine the friction coefficients of the hybrid friction model. The strategy adopted, represented in Fig. 5, was based on an iterative analysis that aims to minimise the total average error of the predicted cutting forces and temperature. This procedure was stopped when the total average error was lower than 10%.

The calibration procedure was carried out for two cutting conditions corresponding to the following cutting parameters:  $V_c = 1000\text{m/min}$  and  $V_c = 1500\text{m/min}$  with  $f = 0.1\text{mm/rev}$ , and  $V_c = 1500\text{m/min}$  with  $f = 0.3\text{mm/rev}$  and both the cooling strategy, namely dry and cryogenic were taken into account during the calibration. At the end of the calibration procedure, through fitting procedure, the general polynomial models representative of  $m$  and  $\mu$  friction coefficients depending on cutting speed and feed rate were determined by MATLAB. Eqs. 20, 21 and 22 permitted to calculate the friction coefficients referred to all the case studied.

$$m_{dry} = 2.625 + 0.25f - 0.0033V_c + 3.432e - 17fV_c + 1.2e - 06V_c^2$$

20

$$\mu_{dry} = 2.612 + 0.9917f - 0.00335V_c - 0.0005fV_c + 1.24e - 06V_c^2$$

21

$$m_{cryo}, \mu_{cryo} = 0.2533 + 0.8583f - 0.00031V_c - 0.0003fV_c + 1.2e - 07V_c^2$$

22

The  $m$  and  $\mu$  computed values related to the dry and cryogenic machining conditions are reported in Table 2.

Table 2  
Calibrated friction coefficient depending on the cutting parameters.

<b>Vc / f</b>	<b>m</b>	<b>μ</b>
1000/0.1	0.55	0.55
1250/0.1	0.4	0.4
1500/0.1	0.4	0.4
1000/0.3	0.6	0.65
1250/0.3	0.45	0.47
1500/0.3	0.45	0.45

As showed by Table 2, the friction coefficients related to the dry machining were affected by the cutting speed and the feed rate. In detail, the high feed rate led to higher friction coefficients while at fixed feed rate, when the cutting speed increased the friction coefficients decreased. The friction coefficients referred to the cryogenic machining were lower than the ones calibrated in dry conditions. The feed rate and cutting speed played the same role observed in dry machining simulations. These numerical results referred to the dry and cryogenic conditions showed similar trends reported also by Cabanettes et al. 2016 operating under dry and lubricated conditions. They observed a decreasing of the friction coefficient when cutting speed increased. The lower friction coefficients reported for cryogenic machining agreed with the experimental observations, in fact lower cutting forces as well as rake face wear due to the reduced tool-chip contact were observed [38].

## 5. Results And Discussion

At the end of the calibration phase where the friction coefficients and the models were determined, the validation phase was carried out in order to understand the reliability of the developed and proposed FE model. The validation was performed taking into account all the case studied, therefore all the machining tests were simulated. The friction coefficients, namely,  $m$  and  $\mu$ , were obtained using the polynomial expressions reported in Eqs. 20, 21 and 22.

### 5.1. FE Validation, cutting forces and temperature prediction

The predicted cutting forces and temperatures depending on the cutting speed, feed rate and manufacturing conditions (dry or cryogenic) were collected and compared with the experimental ones. The results of the comparison of the predicted cutting forces (main and feed force) under dry and cryogenic machining are reported in Figs. 6 and 7.

The maximum temperature was measured considering the same surface evaluated by the analysis of the IR signals acquired by the IR camera [39]. The temperature in this particular area was measured once the temperature distribution depending on the simulated steps reached the steady state condition. Therefore, different values of temperature were measured, and the average value was considered and compared with the experimental one (Fig. 8a and 8b). The FE developed model correctly predicted the experimental temperature as well as the trends at varying cutting speeds, feed rate and cooling strategy. This result is very important because the temperature plays an important role in tool wear phenomena, therefore, the right prediction of this state variable might be used to suggest if the machining strategy is critical for the tool life without performing long and expensive experimental tests.

The developed physics based model was able to successfully predict the main fundamental variables as cutting forces and temperatures as showed by the figures. Between the cutting forces, the main cutting components that is directly related with the power consumption was correctly predicted at varying cutting parameters and cooling conditions. The highest errors in predicting the main cutting components were

2.9% and 3.9% obtained in dry and cryogenic machining simulations respectively, while the other comparison provided an error lower than 1%.

The predicted feed components (Fig. 6b, Fig. 7b) were always smaller than the experimental measurements. This problem was mainly due to the cutting-edge approximation. Indeed, the cutting-edge radius was very small, close to 40  $\mu\text{m}$ , and the elements number required to properly approximate the round shape in 3D dimension was high leading to longer computational time. However, machining parameters as energy or power requirements are mainly related to the main cutting components that were properly predicted, therefore, the poor prediction capability of the feed components is abundantly accepted. Moreover, the error in predicting the feed force did not exceed the 25% and the trend variation at varying cutting parameters and cooling strategy was well predicted. To improve the prediction of this other cutting component, more elements are necessary to approximate the cutting edge round shape, drastically increasing the duration of the simulations. Finally, although a quantitative complete analysis of the chip was not carried out, in Fig. 9 the predicted chip morphology is compared with the experimental obtained during the dry machining test with cutting speed of 1000m/min and feed rate of 0.3mm/rev. The FE model was capable to predict not only the curly shape of the chip during its formation but also the geometrical aspect. The possibility to predict the real dynamic of chip formation can be used to predict other important information as cutting lengths to approximately estimate the tool wear regions related to the tool-chip contact.

## **5.2. Effect of the machining and the LN2 on the surface integrity**

The developed FE model allowed predicting the metallurgical alteration usually triggered when critical conditions (e. g. high strain rate, significant plastic strain and high thermal gradient) are reached during the machining process.

### **5.2.1. Grain size and dislocation density variations**

The equations implemented in the numerical model allowed studying the evolution of the metallurgical changes due to the thermo-mechanical loads induced by the interaction tool-workpiece. The microstructural alteration was predicted on machined surface and inside the workpiece at varying cutting parameters and cooling conditions. In Fig. 10 is shown the top view of the machined surface and the grain size prediction. The white box represents the region in which the grain size was evaluated. For each case study simulated, 60 measurements were carried out and the average value are showed in Fig. 10a and Fig. 10b. The developed model was able to correctly predict the grain refinement due to the machining process. In fact, the grain size numerically predicted was very close to the experimental measured and at varying cutting parameters as well as cooling conditions, the trend was well predicted. Therefore, the FE model can be used to estimate the amount of grain refinement modifying the cutting parameters depending on the machining strategy.

As previously mentioned, the FE model can predict the grain refinement gradient into the subsurface as showed by Fig. 11. A transversal plane cut the machined components, consequently, the internal grain refinement predicted was visible. The metallurgical alteration was well described by the model, since the dislocation density variation was also predicted. Furthermore, the grain refinement in subsurface permitted to understand the amount of the affected layer. Therefore, considering the grain size changes in depth, the thickness of the altered material can be also evaluated and compared with the experimental results.

It is also important to highlight that the cooling conditions coupled with the cutting parameters play a key role in changing the hardness of the machined parts. The analyses showed that the cryogenic fluids promoted the presence of precipitates. As reported by [14], the regions with high dislocations density, due to the plastic deformation accumulation, represent nucleation sites for precipitates. Therefore, a higher percentage of precipitate suggests high dislocation density accumulation. Moreover, the cryogenic temperature annihilated the recovery phenomena, therefore the size of the new recrystallized grains was smaller compared with the one observed on the dry machined samples. The FE developed model permitted to observe the previously mentioned metallurgical phenomena. Indeed, in Fig. 12 the density of the smaller grains in the cryogenic machined part is higher than the one observed on the dry machined one. Moreover, in Fig. 13 the higher dislocation density was predicted on the cryogenic machined sample. The metallurgical phenomena and their evolution can be studied through the FE developed model as well as their contribution to the strengthening of the alloy. The higher dislocation density predicted by the cryogenic simulation, even if not compared with the experimental results, clearly suggests that the low temperature on the machined surface can prevent the presence of recovery effects.

## 6. Conclusion

This work described the development and validation of a FE model to study the effects on the machinability, microstructure and metallurgical features variations (dislocation density) of the aluminium alloy AA7076-T6 when high speed machined under dry and cryogenic conditions. The model can properly predict fundamental industrial relevant information such as the cutting forces that are directly related to the power consumption of the process as well as the thermal field (maximum temperature within the cutting zone). Moreover, as experimentally observed by the authors in another scientific study [39], the microstructural changes mainly represented by small equiaxial grain formation was considered in the development of the numerical model. The FE model was also able to predict the recrystallized grains due to the severity of the machining operation and it also predicted the dislocation density variation induced by the combination of high strain rate, plastic strain, and high temperature and grain size changes.

The following results can be summarised:

- The FE model can accurately predict the cutting forces components (main cutting and feed force) depending on the cutting speed, speed rate and machining conditions i.e. dry or cryogenic. While the prediction of the main cutting force was represented by a very small average error (the maximum

measured was 0.1% and 0.3% for the dry and cryogenic machining respectively), the error increased when the feed force component was considered (30% and 35% for the dry and cryogenic machining respectively). The higher error in predicting the feed force is mainly due to the cutting edge radius that was not properly approximated with the right number of element. However, the prediction of this component does not affect the estimation of the power consumption that is mainly related to the main cutting component. An increase of the elements to better shape the cutting edge will improve the prediction of this variable although the computational time will be significantly increased.

- The thermal field distribution and the maximum temperature within the cutting zone are properly predicted and the numerical results follow the experimental trends.
- The microstructural changes due to the machining operation and the effect of the cooling due to the presence of the LN<sub>2</sub> are computed by the FE model and the prediction allowed to estimate the grain size changes on the machined surface. The measured results are very close to the experimental measurements and the use of LN<sub>2</sub> allowed to preserve the finer recrystallized grains due to the rapid cooling effect.
- The variation of the dislocation density induced by the high plastic strain accumulation, high thermal field and microstructural changes was properly predicted by the model. Although no direct comparison with experimental evidence is reported, a higher accumulation of dislocations due to the rapid cooling effect induced on the cryogenic machined samples was expected as noticed by the XRD analysis [39].

Thus, the proposed work can give a direct answer to the need of properly predict physical phenomena occurring during machining of AA7075 alloy with a consequent high impact in its applicability at an industrial level.

## Declarations

**Authors Contributions:** All the authors contributed to the study conception and design. The development of the numerical model, implementation and analysis was performed by Stano Imbrogno. The manuscript was written by Stano Imbrogno and Giovanna Rotella. Antonio Del Prete reviewed and edited the manuscript. All the authors read and approved the final manuscript.

**Funding:** Not applicable.

**Availability of data and material:** The datasets and the developed codes are available from the corresponding author on reasonable request.

**Ethical approval:** Not applicable.

**Consent to participate:** Not applicable.

**Consent for publication:** The manuscript is approved by all the authors for publication; all the authors listed have approved the manuscript that is enclosed.

**Conflict of interest:** The authors declare no competing interests.

## References

- [1] G. Rotella, O.W. Dillon, D. Umbrello, L. Settineri, I.S. Jawahir, Finite element modeling of microstructural changes in turning of AA7075-T651 Alloy, *Journal of Manufacturing Processes*, Volume 15, Issue 1, 2013, pp. 87-95, ISSN 1526-6125.
- [2] Furumoto, T., Abe, S., Yamaguchi, M. et al. Improving surface quality using laser scanning and machining strategy combining powder bed fusion and machining processes. *Int J Adv Manuf Technol* 117, 3405–3413 (2021).
- [3] Calamaz, M., Coupard, D., Nouari, M. et al. Numerical analysis of chip formation and shear localisation processes in machining the Ti-6Al-4V titanium alloy. *Int J Adv Manuf Technol* 52, 887–895 (2011). <https://doi.org/10.1007/s00170-010-2789-x>
- [4] Ravindranadh Bobbili, Vemuri Madhu, A modified Johnson-Cook model for FeCoNiCr high entropy alloy over a wide range of strain rates, *Materials Letters*, 218, 2018, pp. 103-105, <https://doi.org/10.1016/j.matlet.2018.01.163>.
- [5] M. Alitavoli, A. Darvizeh, M. Moghaddam, P. Parghou, R. Rajabiehfard, Numerical modeling based on coupled Eulerian-Lagrangian approach and experimental investigation of water jet spot welding process, *Thin-Walled Structures*, Volume 127, 2018, pp. 617-628, ISSN 0263-8231, <https://doi.org/10.1016/j.tws.2018.02.005>.
- [6] S. Imbrogno, G. Rotella, S. Rinaldi, Surface and subsurface modifications of AA7075-T6 induced by dry and cryogenic high speed machining, *The International Journal of Advanced Manufacturing Technology* volume 107: 905–918 (2020)
- [7] K. Ma, H. Wen, T. Hu, T. D. Topping, D. Isheim, D. N. Seidman, E. J. Lavernia, J. M. Schoenung, (2014), Mechanical behavior and strengthening mechanisms in ultrafine grain precipitation-strengthened aluminum alloy, *Acta Materialia*, 61: 141-155.
- [8] M. Dixit, R. S. Mishra, K. K. Sankaran, (2008), Structure–property correlations in Al 7050 and Al 7055 high-strength aluminum alloys, *Materials Science and Engineering A*, 478: 163–172.
- [9] Y. H. Zhao, X. Z. Liao, Z. Jin, R. Z. Valiev, Y. T. Zhu, (2004), Microstructures and mechanical properties of ultrafine grained 7075 Al alloy processed by ECAP and their evolutions during annealing, *Acta Materialia*, 52: 4589-4599.
- [10] U.F. Kocks, A statistical theory of flow stress and work-hardening, *Philosophical Magazine*, 13 (1966), pp. 541-566

- [11] S. N. Melkote, R. Liu, P. F. Zelaia, T. Marusich, (2015), A physically based constitutive model for simulation of segmented chip formation in orthogonal cutting of commercially pure titanium, *Cirp Annals*, 64: 65-68.
- [12] I. Sabirov, M. Y. Murashkin, R. Z. Valiev, (2013), Nanostructured aluminium alloys produced by severe plastic deformation: New horizons in development, *Materials Science and Engineering A*, 560: 1-24.
- [13] T.D. Topping, B. Ahn, Y. Li, S.R. Nutt, E.J. Lavernia, (2012), Influence of Process Parameters on the Mechanical Behavior of an Ultrafine-Grained Al Alloy, *Metallurgical and Materials Transactions A*, 43: 505-519.
- [14] J. Gubicza, I. Schiller, N.Q. Chinh, J. Illy, Z. Horita, T.G. Langdon, (2007), The effect of severe plastic deformation on precipitation in supersaturated Al-Zn-Mg alloys, *Materials Science and Engineering A*: 461: 77-85.
- [15] H. Frost, M. Ashby, (1977b), Deformation-mechanism maps for pure iron, two austenitic stainless steels and a low-alloy ferritic steel. In: Jaffee, R.I., Wilcox, B.A. (Eds.), *Fundamental Aspects of Structural Alloy Design*. Plenum Press, pp. 26-65.
- [16] H. Conrad, (1970), The athermal component of the flow stress in crystalline solids, *Material Science and Engineering A*, 6: 265-273.
- [17] E. Arzt, Size effects in materials due to microstructural and dimensional constraints: a comparative review, *Acta Materialia*, 46 (16): 5611-5626.
- [18] A. Seeger, (1956) The mechanism of Glide and Work Hardening in FCC and HCP Metals. In: Fisher, J., Johnston, W.G., Thomson, R., Vreeland, T.J. (Eds.), *Dislocations and Mechanical Properties of Crystals*, pp. 243-329.
- [19] Y. Bergström, (1983), The plastic deformation of metals - A dislocation model and its applicability. *Reviews on powder metallurgy and physical ceramics* 2/3: 79-265.
- [20] D. Holt, (1970), Dislocation cell formation in metals, *Journal of Applied Physics*, 41: 3197-3201.
- [21] T. L. Johnson, C. E. Feltner, Grain size effects in the strain hardening of polycrystals, *Metallurgical and Materials Transactions B* volume 1, 1161 (1970)
- [22] A. V. Lubarda, On Atomic Disregistry, Misfit Energy, and the Peierls Stress of a Crystalline Dislocation, *THE MONTENEGRIN ACADEMY OF SCIENCES AND ARTS PROCEEDINGS OF THE SECTION OF NATURAL SCIENCES*, 17, 2007
- [23] S. Takeuchi (2001), The mechanism of the inverse Hall-Petch relation of nanocrystals, *Scripta Materialia* Volume 44 (8-9): 1483-1487.

- [24] R. O. Scattergood, C. C. Kock, (1992), A modified model for Hall-Petch behavior in nanocrystalline materials, *Scripta Metallurgica et Materialia*, 27: 1195-1200.
- [25] G. J. Thomas, R.W. Siegel, J.A. Eastman, (1990), Grain boundaries in nanophase palladium: high resolution electron microscopy and image simulation, *Scripta Metallurgica et Materialia*, 24: 201-206.
- [26] H. Hallberg, M. Wallin, M. Ristinmaa, (2010), Modelling of continuous dynamic recrystallization in commercial-purity aluminum, *Materials Science and Engineering A*, 527: 1126–1134.
- [27] G. Z. Quan, Y. P. Mao, G. S. Li, W. Q. Lv, Y. Wang, J. Zhou, (2012), A characterization for the dynamic recrystallization kinetics of as-extruded 7075 aluminum alloy based on true stress–strain curves, *Computational Material Science*, 55: 65-72.
- [28] C. Shi, W. Mao, X. G. Chen, (2013), Evolution of activation energy during hot deformation of AA7150 aluminum alloy, *Materials Science and Engineering A* 571: 83-91.
- [29] D. Caillard, J. L. Martin, (2003), *Thermally Activated Mechanisms in Crystal Plasticity*, Pergamon, Oxford.
- [30] H. Frost, M. Ashby, (1982), *Deformation-mechanism maps - the plasticity and creep of metals and ceramics*, Pergamon Press, Oxford.
- [31] M. Nicolas, A. Deschamps, (2003), Precipitate Microstructures and Resulting Properties of Al-Zn-Mg Metal Inert Gas–Weld Heat-Affected Zones, *Metallurgical and Materials Transactions A*, 35: 1437-1448
- [32] O. Ryen, O. Nijs, E. Sjolander, B. Holmedal, H.E. Ekstrom, E. Nes, (2006), Strengthening mechanisms in solid solution aluminum alloys, *Metallurgical and Materials Transactions A*, 37: 1999-2006.
- [33] V. P. Astakhov, S. Joksch, (2012), *Metalworking fluids (MWFs) for cutting and grinding – fundamentals and recent advances: 147–151*; Cambridge, UK, Woodhead Publishing Limited, 1.
- [34] F. Pušavec, T. Lu, C. Courbon, J. Rech, U. Aljancic, J. Kopac, I. S. Jawahir, (2016), Analysis of the influence of nitrogen phase and surface heat transfer coefficient on cryogenic machining performance, *Journal of Materials Processing Technology*, 233: 19-28.
- [35] A. Bordin, S. Imbrogno, G. Rotella, S. Bruschi, A. Ghiotti, D. Umbrello, Finite Element Simulation of Semi-finishing Turning of Electron Beam Melted Ti6Al4V Under Dry and Cryogenic Cooling *Procedia CIRP*, 31 (2015), pp. 551-556.
- [36] T. Özel, (2006), The influence of friction models on finite element simulations of machining, *International Journal of Machine Tools and Manufacture*, 46: 518–530.
- [37] P. J. Arrazola, T. Özel, (2010), Investigations on the effects of friction modeling in finite element simulation of machining, *International Journal of Mechanical Sciences*, 52: 31-42.

[38] F. Cabanettes, J. Rolland, F. Dumont, J. Rech, Z. Dimkovski, (2016), Influence of Minimum Quantity Lubrication on friction characterizing tool-aluminum alloy contact, *Journal of Tribology*, 138: 1-10.

[39] S. Imbrogno, G. Rotella, S. Rinaldi (2020), Surface and subsurface modifications of AA7075-T6 induced by dry and cryogenic high speed machining, *The International Journal of Advanced Manufacturing Technology*, 107: 905–918.

## Figures



### Figure 1

Comparison between the experimental and predicted true stress-strain curves of the aluminium alloy *7075-T6* at varying temperature and strain rate; a) strain-rate  $0.1\text{s}^{-1}$   $T= 200^{\circ}\text{C}$ , b) strain-rate  $0.5\text{s}^{-1}$   $T= 150^{\circ}\text{C}$ .

### Figure 2

Numerical strategy developed to model the mechanical behaviour of the *AA7075-T6* through physically based modelling approach.

**Figure 3**

a) kinematic boundary conditions, remeshing window and  $h_{cryo}$  window definition, b) thermal boundary conditions.

**Figure 4**

heat transfer coefficient implemented in the FE software (Nitrogen properties at  $10^5$  Pa isobar collected and adapted from Pušavec et al. 2016 [34]).

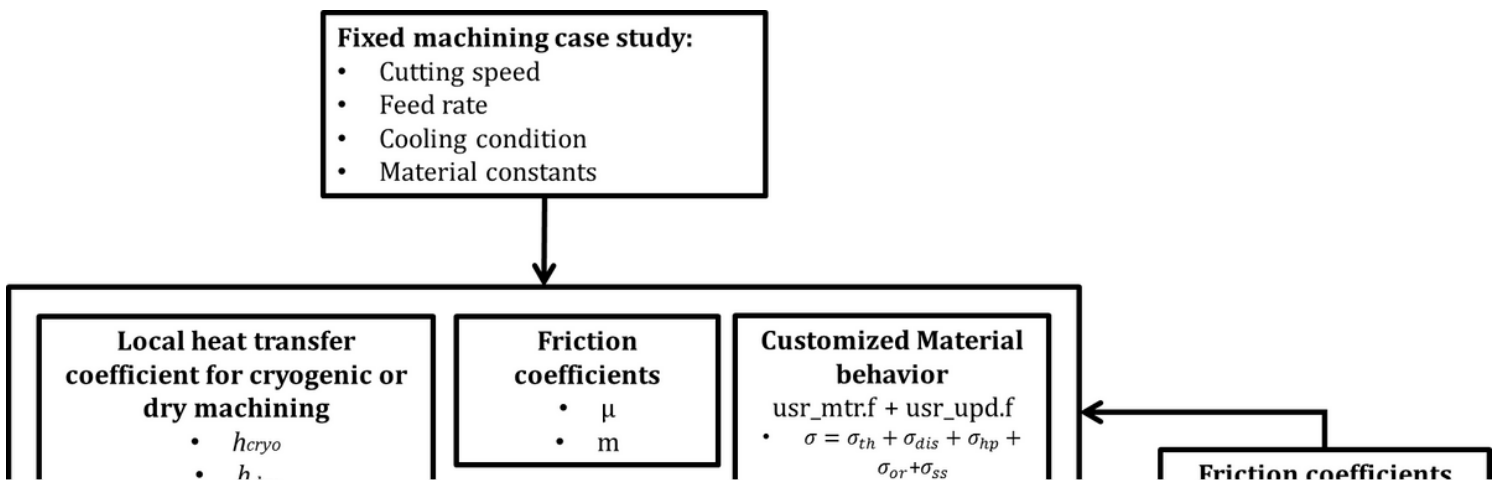


**Figure 5**

Calibration procedure to determine the friction coefficients of the hybrid friction model.

## Figure 6

Comparison between experimental and numerical cutting forces; a) main cutting force ( $F_z$ ) and b) feed forces ( $F_t$ ) under dry conditions.

## Figure 7

Comparison between experimental and numerical cutting forces; a) main cutting force ( $F_z$ ) and b) feed forces ( $F_t$ ) under cryogenic conditions.

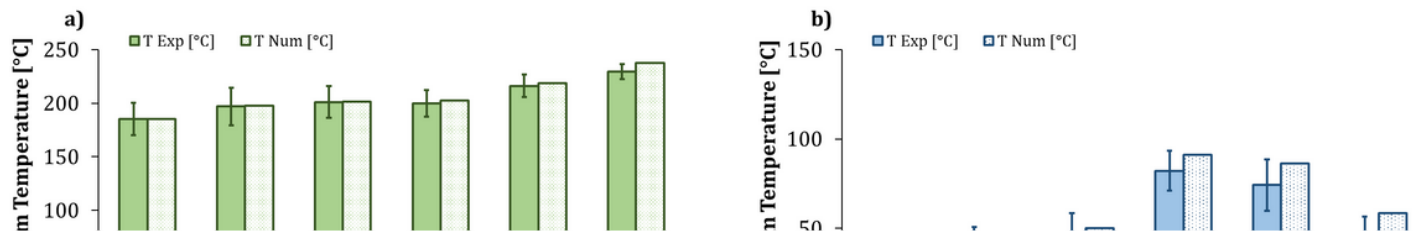


## Figure 8

Comparison between experimental and numerical temperature; a) dry machining and b) cryogenic machining.

## Figure 9

Comparison between the numerical and experimental chip shape ( $V_c=1000\text{m/min}$ ,  $f=0.3\text{mm/rev}$ , dry conditions).

## Figure 10

Predicted microstructure under dry conditions ( $V_c=1500\text{m/min}$ ,  $f=0.3\text{mm/rev}$ ); a) comparison of numerical and experimental grain size measured on machined surface (dry conditions); b) comparison of numerical and experimental grain size measured on machined.

### Figure 11

Grain refinement and dislocation density variations from the machined surface and in depth into the part ( $V_c=1500\text{m/min}$ ,  $f=0.3\text{mm/rev}$ , dry condition)

### Figure 12

Recrystallized grain size prediction at varying cooling conditions ( $f=0.3\text{mm/rev}$ ).

### Figure 13

Dislocation density prediction at varying cooling conditions ( $f=0.3\text{mm/rev}$ ).